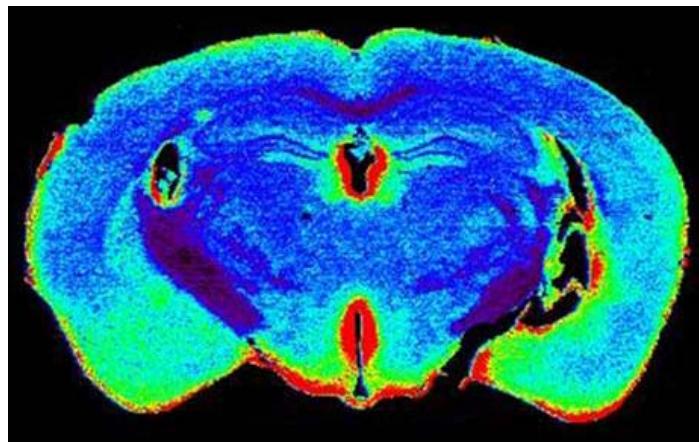


# **Instrumental considerations and applications of elemental bio-imaging**

by Jessica Lear



A thesis submitted for the  
Degree of Doctor of Philosophy (Science)  
University of Technology, Sydney

2012

## **Certificate of authorship and originality**

I certify that the work in this thesis has not previously been submitted for a degree nor has it been submitted as part of the requirements for a degree except as fully acknowledged within the text.

I also certify that the thesis has been written by me. Any help that I have received in my research work and the preparation of the thesis itself has been acknowledged. In addition, I certify that all the information sources and literature used are indicated in the thesis.

Jessica Lear

For Peter and Phyllis

## **Acknowledgements**

Although it's just my name that appears on the cover page, there are a number of people who have been a part of this project's evolution either by direct involvement, funding or support, or simply buying me caffeinated beverages and sugary goodness.

Firstly, I'd like to acknowledge and thank Prof Philip Doble for his supervision, guidance and support throughout the project. His expert knowledge and enthusiasm for analytical chemistry was the reason I shifted towards this field in chemistry and decided to dedicate the last three years to this subject. His excitement regarding my work often exceeded my own and gave me the motivation to continue. His support has resulted in this project providing me with a great deal of experience which is not limited to chemistry.

My co-supervisor, Dr Dominic Hare, has also provided a great deal of support and his experience in all things ICP-MS was extremely useful. His assistance throughout the project has enabled me to complete the work in this timeframe as his expertise provided a solid foundation for the instrumental analyses. His feedback is always greatly appreciated and has helped transform my writing into a mature, academic and fit-for-purpose style.

I'd like to thank the members of the ICP-MS research group including Christine Austin, Amanda Van Gramberg and Alison Beavis for their support and help throughout the project. Thank you to Christine for using the ICP-MS before me so many times and tuning it wonderfully, and Amanda for listening to my thoughts about instrument functionality. Also thank you to Ilona Kramer and David Bishop for running the labs so efficiently. Dave's help was always greatly appreciated.

I'd like to mention and thank Fred Fryer from Agilent Technologies for providing unmatched experience and expertise in the ICP-MS field and allowing me to soak it all in.

Thank you to my collaborators, Paul Adlard and David Finkelstein at the MHRI, and Stephen Robinson from Monash University for the preparation of my brain samples and their expert interpretations of the results.

I'd also like to thank all of my friends for their support throughout this project. They have provided some wonderful memories and have allowed me to escape the clutches of monotonous data analyses with the consumption of cocktails and dumplings (not together).

Thank you to my family who have always been supportive of my undertakings. They're probably one of the least stressful families to be a part of. My parents have provided me with significant financial support over the years and I'd like to thank them for letting me invade their house again while I've had no idea what's happening with my career now I'm at the end of my PhD (and scholarship).

The final thank you goes to Rami Paul. I met him a week before I started my project and he has been there for me throughout. Rami's ability to take my mind off the project's more stressful aspects can't be matched and I appreciate every single little thing he has brought to my life.

# Table of Contents

<b>CERTIFICATE OF AUTHORSHIP AND ORIGINALITY .....</b>	<b>II</b>
<b>ACKNOWLEDGEMENTS .....</b>	<b>IV</b>
<b>LIST OF FIGURES .....</b>	<b>XI</b>
<b>LIST OF TABLES .....</b>	<b>XVIII</b>
<b>LIST OF PUBLICATIONS.....</b>	<b>XXII</b>
<b>LIST OF CONFERENCE PRESENTATIONS.....</b>	<b>XXIII</b>
<b>ABBREVIATIONS .....</b>	<b>XXIV</b>
<b>ABSTRACT .....</b>	<b>XXVI</b>
<b>CHAPTER 1: INTRODUCTION.....</b>	<b>2</b>
1.1    ELEMENTAL BIO-IMAGING .....	2
1.2    LA-ICP-MS .....	2
1.2.1    Inductively coupled plasma - mass spectrometry.....	3
1.2.1.1    Inductively coupled plasma ion source.....	4
1.2.1.2    Mass spectrometry .....	6
1.2.1.2.1    Mass analysers.....	7
1.2.1.2.2    Mass detectors .....	10
1.2.2    Laser ablation.....	12
1.2.2.1    Lasers used in LA-ICP-MS .....	13
1.2.2.2    Ablation cell dynamics .....	16
1.2.3    Considerations for LA-ICP-MS.....	20
1.2.3.1    Elemental fractionation .....	20
1.2.3.2    Interferences.....	21
1.3    IMAGING USING LA-ICP-MS .....	25
1.3.1    Imaging methods.....	29
1.3.2    Quantification strategies.....	30

---

1.3.3	<i>Future direction of EBI</i> .....	35
1.4	PROJECT AIMS.....	36
<b>CHAPTER 2:</b>	<b>EXPERIMENTAL</b> .....	<b>38</b>
2.1	INSTRUMENTATION .....	38
2.1.1	<i>Inductively coupled plasma – mass spectrometer</i> .....	38
2.1.2	<i>Laser ablation</i> .....	39
2.1.3	<i>Solution ICP-MS operational parameters</i> .....	40
2.1.4	<i>LA-ICP-MS operational parameters</i> .....	41
2.2	DATA ACQUISITION AND PROCESSING.....	44
2.2.1	<i>Data acquisition</i> .....	44
2.2.2	<i>Data manipulation</i> .....	48
2.2.2.1	Normalisation and data organisation .....	48
2.2.2.2	Background subtraction.....	50
2.2.3	<i>Image construction</i> .....	51
2.3	EXPERIMENTAL METHODS.....	53
2.3.1	<i>Tissue standard preparation</i> .....	53
2.3.1.1	Microwave assisted acid digestion .....	56
2.3.1.2	Solution ICP-MS analysis.....	57
2.3.1.3	Tissue sectioning.....	58
2.3.1.4	LA-ICP-MS calibration .....	59
2.4	CALCULATIONS .....	61
2.4.1	<i>Linear regression analysis</i> .....	61
2.4.2	<i>Limits of analysis</i> .....	62
2.4.3	<i>Signal to noise ratios</i> .....	62
2.5	ANIMALS.....	63
2.5.1	<i>ZnT3 KO mouse brains</i> .....	63
2.5.2	<i>PBT-2 treated ZnT3 KO mice</i> .....	64

---

2.5.3	<i>AGE/Intermittent hypoxic mice</i> .....	65
<b>CHAPTER 3:</b>	<b>IMPROVING MATRIX-MATCHED TISSUE STANDARD PREPARATION</b> .....	<b>68</b>
3.1	CHAPTER OUTLINE.....	68
3.2	TISSUE HOMOGENEITY .....	70
3.3	CALIBRATION DATA .....	74
3.3.1	<i>SN-ICP-MS</i> .....	74
3.3.2	<i>LA-ICP-MS</i> .....	78
3.4	COMPARISON OF CALIBRATION DATA .....	81
3.5	CONCENTRATION RANGE AND NUMBER OF ANALYTES .....	82
3.6	CONCLUSIONS.....	84
<b>CHAPTER 4:</b>	<b>INCREASING IMAGE ACQUISITION SPEED</b> .....	<b>86</b>
4.1	CHAPTER OUTLINE.....	86
4.2	IMAGE CONSTRUCTION .....	88
4.3	LIMITATIONS TO SCAN CYCLE .....	90
4.4	LIMITS OF ANALYSIS.....	93
4.5	SIGNAL CARRY-OVER EXPERIMENTS.....	95
4.6	LASER FLUENCE .....	99
4.7	IMAGING WITH INCREASED LASER SCAN SPEED .....	99
4.7.1	<i>Background subtraction</i> .....	106
4.7.2	<i>Maintaining image dimensions</i> .....	108
4.8	CONCLUSIONS.....	109
<b>CHAPTER 5:</b>	<b>APPLICATIONS OF INCREASED SPEED ELEMENTAL BIO-IMAGING</b> .....	<b>111</b>
5.1	CHAPTER OUTLINE.....	111
5.2	BACKGROUND.....	112
5.2.1	<i>Neurodegeneration</i> .....	112
5.2.2	<i>Alzheimer's disease</i> .....	115
5.2.2.1	<i>AD pathogenesis</i> .....	115



---

5.3	APPLICATION 1: THE EFFECT OF PBT-2 ON METAL DISTRIBUTION IN THE BRAINS OF ZNT3 KO MICE.....	120
5.3.1	Outline.....	120
5.3.2	Treatment strategies for AD.....	121
5.3.3	ZnT3 knockout mice.....	125
5.3.4	Zinc deficits in ZnT3 KO animals.....	126
5.3.5	PBT-2 treated animals.....	129
5.3.5.1	Zinc.....	130
5.3.5.2	Other elements.....	133
5.4	APPLICATION 2: THE EFFECT OF AGES AND SLEEP APNOEA ON THE DISTRIBUTION OF METALS IN THE BRAIN	136
5.4.1	Outline.....	136
5.4.2	Advanced glycation end-products.....	138
5.4.3	Sleep apnoea and AD.....	143
5.4.4	Imaging.....	143
5.4.4.1	Effectiveness of the speed equation.....	145
5.4.4.2	Cobalt.....	146
5.4.4.3	Other elements.....	149
5.5	CONCLUSIONS.....	152
<b>CHAPTER 6:</b>	<b>USING H<sub>2</sub> REACTIVE GAS TO IMPROVE SENSITIVITY FOR EBI.....</b>	<b>154</b>
6.1	CHAPTER OUTLINE.....	154
6.2	RESTRICTIONS TO HIGH RESOLUTION EBI.....	156
6.3	THE REACTION CELL AND HYDROGEN AS A REACTIVE GAS.....	157
6.4	BACKGROUND LEVELS OF BIOLOGICALLY RELEVANT ANALYTES.....	162
6.5	CALIBRATION USING INCREASING VOLUMES OF HYDROGEN.....	165
6.5.1	Limits of analysis.....	166
6.5.2	Sensitivity.....	168
6.6	IMAGING USING INCREASING VOLUMES OF HYDROGEN.....	170
6.7	CONCLUSIONS.....	176

---

<b>CHAPTER 7: HIGH RESOLUTION IMAGING EMPLOYING H<sub>2</sub> REACTIVE GAS</b> .....	<b>178</b>
7.1 CHAPTER OUTLINE.....	178
7.2 PARKINSON'S DISEASE AND THE SUBSTANTIA NIGRA .....	179
7.3 IMAGING IRON AT HIGH RESOLUTION .....	181
7.3.1 <i>Images</i> .....	182
7.3.2 <i>Calibration</i> .....	186
7.4 CONCLUSION .....	190
<b>CHAPTER 8: CONCLUSIONS AND RECOMMENDATIONS</b> .....	<b>192</b>
<b>APPENDIX</b> .....	<b>197</b>
<b>REFERENCES</b> .....	<b>200</b>

## List of figures

Figure 1-1: Analysis by ICP-MS.....	3
Figure 1-2: Schematic of ICP-MS interface [13; 14] .....	4
Figure 1-3: Formation of the inductively coupled plasma [14].....	5
Figure 1-4: Mechanism of conversion of a droplet to a positive ion in the ICP [14] .....	6
Figure 1-5: Diagram of a quadrupole mass analyser showing ion paths [22].....	9
Figure 1-6: Schematic of a discrete dynode electron multiplier [14] .....	11
Figure 1-7: Schematic of a typical Nd:YAG laser ablation unit [23] .....	12
Figure 1-8: Four energy level diagram for Nd <sup>3+</sup> ions in a Nd:YAG laser. Lasing occurs between the metastable levels [13; 25] .....	14
Figure 1-9: Schematic of a standard laser ablation cell [13].....	17
Figure 1-10: Schematic of the large format laser ablation cell.....	18
Figure 1-11: Particle size distribution after 40 second ablation of 40 µm craters in SRM 612 glass using argon and helium carrier gases [33] .....	19
Figure 1-12: A model for the differences in particle size distribution based on the thermal conductivities of the gases used in LA-ICP-MS [31] .....	20
Figure 1-13: Timeline of EBI .....	28
Figure 1-14: Workflow for imaging using LA-ICP-MS [1] .....	29
Figure 2-1: Agilent 7500ce ICP-MS.....	38
Figure 2-2: New Wave UP213 laser ablation unit fitted with a standard cell.....	39
Figure 2-3: Example of a microscope slide with sections of mouse brain prepared for LA-ICP-MS analysis.....	44

---

Figure 2-4: Representation of imaging experiments. Each line represents a scan file saved as a .csv file according to the numbers on the right.....	45
Figure 2-5: Laser traversing the surface of the sample in a continuous series of pulses, 20 Hz in these experiments .....	45
Figure 2-6: ICP-MS software showing the acquisition parameters and dwell times set for individual m/z .....	46
Figure 2-7: Example of a laser scan file for $^{66}\text{Zn}$ represented as an x-y scatter plot prepared in MS Excel .....	47
Figure 2-8: A single scan file as opened from the saved .csv file.....	48
Figure 2-9: View of organised MS Excel data after utilising a macro in MS Excel .....	49
Figure 2-10: View of the organised MS Excel data after background subtraction. This particular section of data is mostly background so the majority of values are small or equal to zero. ....	50
Figure 2-11: a) Sequential scan files showing signal intensities for $^{66}\text{Zn}$ ; b) Image for $^{66}\text{Zn}$ : the highlighted pixels indicate four sequential scan files .....	52
Figure 2-12: Flow-chart for tissue standard preparation.....	54
Figure 2-13: Acid digestion method.....	57
Figure 2-14: A typical signal profile for a tissue standard.....	59
Figure 3-1: Visual homogeneity of standards prepared using $1000\ \mu\text{g mL}^{-1}$ single element standard solutions as observed through the microscope fitted to the laser ablation unit (500x magnification) .....	70
Figure 3-2: $^{13}\text{C}$ signal intensity during line ablation for tissue standards prepared using $1000\ \mu\text{g mL}^{-1}$ standard single element solutions. Signal moves from gas blank to standard ablation and returns to gas blank. ....	71

---

Figure 3-3: Visual homogeneity of standards prepared using metal salt solutions as observed through the microscope fitted to the laser ablation unit (500x magnification).....	72
Figure 3-4: $^{13}\text{C}$ signal intensity during line ablation for tissue standards prepared using metal salt solutions. Signal moves from gas blank to standard ablation and returns to gas blank...	73
Figure 3-5: Comparison of the relative standard deviations of the $^{13}\text{C}$ signal during ablation of the prepared calibration standards .....	74
Figure 3-6: SN-ICP-MS calibration curves for each analyte in the aqueous standards.....	75
Figure 3-7: LA-ICP-MS calibration curves for each analyte in the tissue standards with error bars at 95% confidence.....	79
Figure 4-1: The effect of varying the laser scan speed on image dimensions .....	88
Figure 4-2: Counts per data point versus the dwell time of the quadrupole MS compared with the limiting signal at each dwell time for selected m/z. ( $v_l = 3 \times \chi_s \mu\text{ms}^{-1}$ ) .....	92
Figure 4-3: Limits of analysis with increasing $v_l$ ( $\chi_s = 30 \mu\text{m}^{-1}$ ).....	94
Figure 4-4: Washout times for a large format laser ablation cell .....	96
Figure 4-5: Comparison of normalised signal intensities for the total ion count (TIC) $\pm$ standard deviations across laser spot diameters and increasing scan speed .....	97
Figure 4-6: Washout times for a standard laser ablation cell.....	98
Figure 4-7: Comparison of laser scan speed and resolution for $^{63}\text{Cu}$ using spot sizes of 15, 30, 65 and 100 $\mu\text{m}$ where each segment broken by a dotted line indicates an increase in laser scan speed.....	102
Figure 4-8: Comparison of laser scan speed and resolution for $^{66}\text{Zn}$ using spot sizes of 15, 30, 65 and 100 $\mu\text{m}$ where each segment broken by a dotted line indicates an increase in laser scan speed.....	103

---

Figure 4-9: Comparison of laser scan speed and resolution for $^{56}\text{Fe}$ using spot sizes of 15, 30, 65 and 100 $\mu\text{m}$ where each segment broken by a dotted line indicates an increase in laser scan speed.....	104
Figure 4-10: Comparison of laser scan speed and resolution for $^{55}\text{Mn}$ using spot sizes of 15, 30, 65 and 100 $\mu\text{m}$ where each segment broken by a dotted line indicates an increase in laser scan speed.....	105
Figure 4-11: Laser scan speed comparison for $^{56}\text{Fe}$ prior to background subtraction ( $x_s = 15 \mu\text{m}$ ).....	106
Figure 4-12: Background drift of the isotopes imaged supporting the need for background subtraction in these experiments.....	107
Figure 4-13: Demonstration of the use of increased $v_l$ while maintaining image dimensions equivalent to the original tissue section ( $x_s = 30 \mu\text{m}$ , $t_{sc} = 0.2372$ seconds and $v_l = 127 \mu\text{m s}^{-1}$ ).....	108
Figure 5-1: Reactive oxygen species generation by redox-active metals as the basis for neurodegenerative disorders that are related to oxidative damage [89].....	112
Figure 5-2: Model for the non-pathogenic metallobiology of $\beta$ -amyloid ( $\text{A}\beta$ ).....	116
Figure 5-3: Model for the metallobiology of $\beta$ -amyloid ( $\text{A}\beta$ ) in Alzheimer's Disease. Proposed sequence of events leading to AD [100].....	119
Figure 5-4: Chemical structure of Clioquinol (CQ).....	123
Figure 5-5: Proposed mechanism of action of clioquinol and similar metal-protein attenuation compounds (MPACs).....	124
Figure 5-6: Comparison of $^{66}\text{Zn}$ distribution in the brains of wild type mice and ZnT3 KO mice ( $x_s = 40 \mu\text{m}$ , $v_l = 40 \mu\text{m s}^{-1}$ ).....	128
Figure 5-7: Regions of interest from where data was extracted; RHS = right hand side, LHS = left hand side, CTX = cortex, Amyg = amygdala, 5 = hippocampus (HIPP), 1-4 = pyramidal layer of the hippocampus (HIPP).....	130

Figure 5-8: Images of $^{66}\text{Zn}$ for PBT-2 treated mouse brains compared to SSV mouse brains ( $x_s = 30 \mu\text{m}$ , $v_l = 120 \mu\text{m s}^{-1}$ ).....	131
Figure 5-9: Concentrations of $^{66}\text{Zn} \pm 95\%$ confidence interval for the selected regions of interest in PBT-2 and SSV mouse brains .....	132
Figure 5-10: Images of $^{63}\text{Cu}$ for PBT-2 treated mouse brains compared to SSV mouse brains ( $x_s = 30 \mu\text{m}$ , $v_l = 120 \mu\text{m s}^{-1}$ ).....	134
Figure 5-11: Images of $^{56}\text{Fe}$ for PBT-2 treated mouse brains compared to SSV mouse brains ( $x_s = 30 \mu\text{m}$ , $v_l = 120 \mu\text{m s}^{-1}$ ).....	135
Figure 5-12: Glucose and AGE formation pathways incorporating the polyol pathway and AGE formation by the $\alpha$ -oxoaldehydes glyoxal, methyl glyoxal and 3-DG. [114] .....	138
Figure 5-13: Formation of advanced glycation end-products (AGEs) starts by a reaction of the amino group of a protein and a reducing sugar (here: glucose) and completed by the reaction between 1,2-dicarbonyl compounds (here: glyoxal and methylglyoxal) and the Amadori product [115] .....	139
Figure 5-14: Structures of methylglyoxal-derived AGEs found in the Alzheimer's disease brain [115].....	142
Figure 5-15: Effectiveness of $v_l = x_s / t_{sc}$ in reproducing images with equivalent dimensions to the original tissue section .....	145
Figure 5-16: $^{59}\text{Co}$ distribution in the brains of LTIH and SIH mice fed low and high AGE diets, and control mice. Black and white images show where the brain sections should be had $^{59}\text{Co}$ been detected.....	147
Figure 5-17: Cobalt in Vitamin B <sub>12</sub> (cobalamin).....	148
Figure 5-18: $^{63}\text{Cu}$ distribution in the brains of LTIH and SIH mice fed low and high AGE diets .....	149
Figure 5-19: $^{66}\text{Zn}$ distribution in the brains of LTIH and SIH mice fed low and high AGE diets .....	150

Figure 5-20: $^{57}\text{Fe}$ distribution in the brains of LTIH and SIH mice fed low and high AGE diets	151
Figure 6-1: Effect of varying $x_s$ on the volume of tissue ablated per laser pulse ( $h = 30 \mu\text{m}$ )	157
Figure 6-2: Schematic of Agilent ICP-MS showing the Octopole Reaction System (ORS) cell	158
Figure 6-3: Comparison of background signals; $\text{Log}_{10}$ (counts per second) versus $\text{H}_2$ flow rate ( $\text{mL min}^{-1}$ )	162
Figure 6-4: Comparison of the slope of calibration curves constructed for $^{56}\text{Fe}$ with increasing $v_1$ and increasing $\text{H}_2$ flow rates in the reaction cell. ( $x_s = 30 \mu\text{m}$ )	166
Figure 6-5: Limits of analysis ( $\mu\text{g g}^{-1}$ ) for calibrated analytes with increasing $\text{H}_2$ flow rates in the reaction cell ( $x_s = 30 \mu\text{m}$ , $v_1 = 90 \mu\text{m s}^{-1}$ )	167
Figure 6-6: Comparison of the LODs (dashed lines) and LOQs (solid lines) for $^{56}\text{Fe}$ and $^{44}\text{Ca}$ for $\text{H}_2$ flow rates of 0 (red) and 3 $\text{mL min}^{-1}$ (blue) against the concentrations of the calibration standards	168
Figure 6-7: Signal (per $\mu\text{g g}^{-1}$ ) to noise ratios (SNR) for the calibrated analytes with increasing $\text{H}_2$ flow rates and increasing $v_1$ . ( $x_s = 30 \mu\text{m}$ , $v_1 = 30$ [○], 60 [■] and $90 \mu\text{m s}^{-1}$ [X])	169
Figure 6-8: Comparison of iron imaged with increasing $\text{H}_2$ flow rates	171
Figure 6-9: Comparison of $^{55}\text{Mn}$ imaged with increasing $\text{H}_2$ flow rates	172
Figure 6-10: Comparison of $^{63}\text{Cu}$ imaged with increasing $\text{H}_2$ flow rates	174
Figure 6-11: Comparison of $^{66}\text{Zn}$ imaged with increasing $\text{H}_2$ flow rates	175
Figure 7-1: Immunohistochemical stain of the right side of a section of mouse brain [1]. The area outlined corresponds to the area containing the SN. The area in the square represents an example of the area analysed in this experiment.	180
Figure 7-2: $^{56}\text{Fe}$ image of the lower left quarter of a mouse brain containing the substantia nigra	183



Figure 7-3: $^{63}\text{Cu}$ image of the lower left quarter of a mouse brain containing the substantia nigra .....	184
Figure 7-4: $^{66}\text{Zn}$ image of the lower left quarter of a mouse brain containing the substantia nigra .....	185
Figure 7-5: Signal to noise ratios for imaged isotopes using 3.0 and 0.0 mL min $^{-1}$ H $_2$ in the reaction cell.....	188
Figure 7-6: Comparison of the calibration data for $^{56}\text{Fe}$ with 3.0 and 0.0 mL min $^{-1}$ H $_2$ .....	189

## List of tables

Table 1-1: Strengths and weaknesses of mass analysers [18] .....	7
Table 1-2: Characteristics of performance of mass analysers [19] .....	8
Table 1-3: Characteristic parameters of selected lasers used for LA-ICP-MS [13] .....	13
Table 1-4: Common polyatomic interferences from biological matrices. Adapted from [41] .	22
Table 1-5: Comparison of background signals measured by LA-ICP-MS and SN-ICP-MS; Adapted from [42] .....	24
Table 1-6: Main spatially resolved analytical techniques for chemical element imaging, quantification, and speciation in biological samples; adapted from [55] .....	26
Table 1-7: Advantages and drawbacks of quantification procedures for EBI [76] .....	32
Table 2-1: Typical operational parameters used during solution ICP-MS analysis using Agilent 7500ce ICP-MS .....	41
Table 2-2: Element concentrations in NIST Glass 612; * denotes certified value [84] .....	42
Table 2-3: Typical laser parameters used during tuning .....	42
Table 2-4: Typical operational parameters during LA-ICP-MS analysis in standard mode using Agilent 7500ce ICP-MS with cs lenses .....	43
Table 2-5: Typical operational parameters during LA-ICP-MS analysis in reaction mode using Agilent 7500ce ICP-MS with cs lenses. The same parameters were used for other volumes of H <sub>2</sub> during the same analysis periods .....	43
Table 2-6: Representation of post-macro data organised into a single MS Excel file in Band Interleave by Line (BIL) format, prepared for interpretation by the ENVI Imaging Suite .....	49
Table 2-7: Soluble metal salts used to prepare high concentration salt solutions (Sigma-Aldrich) .....	54

---

Table 2-8: Approximate volume of concentrated salt solutions spiked into 5.0 g of chicken breast.....	55
Table 2-9: Approximate concentration of elements spiked into chicken breast.....	55
Table 2-10: Concentrations of elements in solution ICP-MS external calibration standards ( $\mu\text{g kg}^{-1}$ ) .....	58
Table 2-11: Functions used for linear regression analysis in Excel and the corresponding calculations performed; where $\bar{y}$ , $\bar{x}$ and $\bar{a}$ are sample averages; $\hat{y}$ is the y-value calculated from the linear regression equation; n is the number of observations; $y_0$ is the average background signal .....	61
Table 2-12: Equations used for determining the limits of analysis; where $y_0$ is the average background signal, $s_0$ is the standard deviation of the background signal, b is the intercept, and m is the slope. ....	62
Table 2-13: Equations used for calculating the signal to noise ratios; where $y_0$ is the average background signal, $y_c$ is the average signal for a mid-range standard, and $x_c$ is the known concentration of that mid-range standard. ....	62
Table 3-1: Errors in the slope and intercept of the SN-ICP-MS calibration curves calculated using linear regression analysis, and the correlation coefficient, detection limit and background equivalent concentration calculated by the ICP-MS software .....	76
Table 3-2: Calculated analyte concentrations in each of the tissue standards prepared using metal salt solutions .....	77
Table 3-3: Errors in the slope and intercept, and the correlation coefficient, detection limit and background equivalent concentration of the LA-ICP-MS calibration curves calculated using linear regression analysis. ....	80
Table 3-4: Comparison of the error in slope, detection limits and correlation coefficient for the standards prepared with $1000 \mu\text{g mL}^{-1}$ solutions and those prepared with the metal salt solutions.....	81
Table 3-5: Volume of standard solutions added to tissue standards before homogenisation	82

---

Table 4-1: LA-ICP-MS operational parameters .....	90
Table 4-2: Selected minimum dwell times for each element in the prepared chicken standards .....	93
Table 4-3: Slopes of the calibration curves with increasing $v_1$ ( $x_s = 30 \mu\text{m}$ ) .....	94
Table 5-1: Organisational framework for the involvement of metals in neurological diseases. The disorders listed are confined to instances where there is a prominent or primary neurological phenotype, and does not address secondary syndromes. Adapted from [89]	114
Table 5-2: Current symptomatic drug therapies for Alzheimer's disease [103-105].....	121
Table 5-3: LA-ICP-MS operational parameters prior to the development of imaging with increased $v_1$ .....	127
Table 5-4: LA-ICP-MS operational parameters .....	129
Table 5-5: P-values from two-tailed t-tests assuming equal variances for the concentration of $^{66}\text{Zn}$ in selected regions of interest between PBT-2 and SSV mice .....	132
Table 5-6: P-values from two-tailed t-tests assuming equal variances for the concentration of $^{63}\text{Cu}$ in selected regions of interest between PBT-2 and SSV mice.....	133
Table 5-7: P-values from two-tailed t-tests assuming equal variances for the concentration of $^{56}\text{Fe}$ in selected regions of interest between PBT-2 and SSV mice .....	133
Table 5-8: Advanced glycation end-product (AGE) content of selected foods prepared by standard cooking methods [119; 120] .....	140
Table 5-9: LA-ICP-MS operational parameters .....	144
Table 5-10: Average concentrations of $^{59}\text{Co}$ in the mouse brain sections.....	146
Table 6-1: Possible reaction pathways that can resolve the analyte from interferences in a reaction cell [162] .....	158
Table 6-2: Important analytes for EBI analysis and their interferences .....	159

---

Table 6-3: LA-ICP-MS operational parameters .....	161
Table 7-1: LA-ICP-MS operational parameters .....	181
Table 7-2: Calibration statistics for isotopes with the use of reaction cell at 3.0 mL min <sup>-1</sup> H <sub>2</sub> , x <sub>s</sub> = 6 μm; v <sub>i</sub> = 16 μm s <sup>-1</sup> .....	186
Table 7-3: Calibration statistics for isotopes with the use of reaction cell at 0.0 mL min <sup>-1</sup> H <sub>2</sub> , x <sub>s</sub> = 6 μm; v <sub>i</sub> = 16 μm s <sup>-1</sup> .....	187

## List of publications

- ❖ Lear, J., Hare, D., Adlard, P., Finkelstein, D., & Doble, P. (2012). Improving acquisition times of elemental bio-imaging for quadrupole-based LA-ICP-MS. *Journal of Analytical Atomic Spectrometry*, 27(1), 159-164.
- ❖ Lear, J., Hare, D., Fryer, F., Adlard, P., Finkelstein, D., & Doble, P. (2012). High-resolution elemental bio-imaging of Ca, Mn, Fe, Co, Cu and Zn employing LA-ICP-MS and hydrogen reaction gas. *Analytical Chemistry*, DOI: 10.1021/ac301156f
- ❖ Lear, J., Veasey, S. C., Zhu, Y., Doble, P., Hare, D., Wang, S., et al. (2012). Long-term Intermittent Hypoxia Results in Cobalt Accumulation in the Brain: Implications for Vitamin B12 in Obstructive Sleep Apnea. *Sleep*, Under Review.
- ❖ Austin, C., Fryer, F., Lear, J., Bishop, D., Hare, D., Rawling, T., Kirkup, L., McDonagh, A., & Doble, P. (2011). Factors affecting internal standard selection for quantitative elemental bio-imaging of soft tissues by LA-ICP-MS. *Journal of Analytical Atomic Spectrometry*, 26(7), 1494-1501.
- ❖ Hare, D., Lear, J., Bishop, D., Beavis, A., & Doble, P. (2012). Protocol for production of matrix-matched brain tissue standards for imaging by laser ablation-inductively coupled plasma-mass spectrometry. *Analytical Methods*, Under Review.
- ❖ Article in preparation by Paul Adlard and David Finkelstein of the Mental Health Research Institute (MHRI), Victoria; *PBT2: A Novel Neuroprotective Agent that Enhances Cognition in Ageing*

## List of conference presentations

- ❖ Lear, J., Hare, D., & Doble, P. (2009). *Elemental bio-imaging of trace elements in neurological disorders: Improving the technique*. Paper presented at the 17th Annual RACI R&D Topics Conference.
  
- ❖ Lear, J., Hare, D., & Doble, P. (2011). *Elemental Bio-imaging: Can acquisition times be improved?* Paper presented at the 3rd International Symposium on Metallomics.

## Abbreviations

µg	Micrograms
µm	Micrometres
AChE	Acetylcholinesterase
AD	Alzheimer's disease
AGE	Advanced glycation end-product
Ar	Argon
As	Arsenic
Aβ	Beta-amyloid
BBB	Blood brain barrier
BuChE	Butyrylcholinesterase
C	Carbon
Ca	Calcium
ChEI	Cholinesterase inhibitor
CNS	Central nervous system
Co	Cobalt
CPS	Counts per second
CQ	Clioquinol
CRM	Certified reference material
Cu	Copper
EBI	Elemental bio-imaging
Fe	Iron
g <sup>-1</sup>	per gram
H	Hydrogen
He	Helium
HNO <sub>3</sub>	Nitric acid
ICP	Inductively coupled plasma
K	Potassium
KO	Knockout
LA-ICP-MS	Laser ablation inductively coupled plasma mass spectrometry
LFC	Large format cell
<i>m/z</i>	Mass –to-charge ratio
MALDI	Matrix-assisted laser desorption/ionization
Mg	Magnesium



---

Mn	Manganese
MPAC	Metal-protein attenuation compound
MPO	Myeloperoxidase
MS	Mass spectrometry
Nd:YAG	Neodymium-doped yttrium aluminium garnet
NFT	Neurofibrillary tangles
Ni	Nickel
NIST	National Institute of Standards and Technology
NMDA	<i>N</i> -methyl-D-aspartate
O	Oxygen
P	Phosphorous
Pb	Lead
PBT-2	A second generation CQ derivative
PD	Parkinson's disease
Rh	Rhodium
RNS	Reactive nitrogen species
ROS	Reactive oxygen species
SRM	Standard reference material
s <sup>-1</sup>	per second
Se	Selenium
SN-ICP-MS	Solution nebulisation inductively coupled plasma mass spectrometry
TOF	Time-of-flight
Zn	Zinc
ZnT3	A synaptic zinc transporter
α <sub>2</sub> M	α <sub>2</sub> -Macroglobulin

## Abstract

Elemental Bio-Imaging (EBI) is an established application of laser ablation inductively coupled plasma mass spectrometry (LA-ICP-MS) that determines spatial distributions of *in situ* trace element concentrations in thin sections of biological tissues. This project provides an examination of instrumental considerations relating to method development and refinement, and the utilisation of amended methods for the analysis of element concentration distributions in specific biological samples.

The first instrumental consideration examined improving the methods used for matrix-matched tissue standard preparation. The main disadvantage to the previously proposed tissue standard preparation was a decrease in the homogeneity of sectioned tissue as the concentrations of spiked elements increased. The decrease in homogeneity was due to the use of relatively low concentration ( $1000 \mu\text{g mL}^{-1}$ ) certified single element standard solutions. Substituting the low concentration solutions for higher concentration solutions, prepared using soluble metal salts, allowed for smaller quantities of solution to be spiked into the tissue. This increased homogeneity and the ability to spike a greater number of analytes into each tissue standard.

The appropriateness of increasing laser scan speed for the reduction of total experimental analysis time was also examined. EBI experiments normally employ scan speeds where the distance traversed in one second is equal to or less than the diameter of the laser beam. Consequently, data for a higher-resolution (pixel size =  $15 \mu\text{m} \times 15 \mu\text{m}$ ) image of a 5 mm x 5 mm tissue section can take upwards of 30 hours to acquire. Appropriate laser scan speeds may be calculated by consideration of the relationship between laser scan speed, laser spot diameter and the total scan cycle of the quadrupole mass analyser. A simple method to

calculate the laser scan speeds capable of reducing the acquisition time by up to a factor of five whilst maintaining dimensional integrity of the image is presented in this thesis.

Two applications were developed utilising increased laser scan speeds. Both applications were related to the study of the neurodegenerative disorder, Alzheimer's disease, and examined particular variables and their effects on the distribution of metals in the brain. The first application examined the effectiveness of a new drug, PBT-2, on the redistribution of elements in mouse brains with the zinc transporter-3 gene removed. Results indicated PBT-2 had little effect on the distribution of  $^{66}\text{Zn}$ ,  $^{63}\text{Cu}$  and  $^{56}\text{Fe}$  in the midbrain. The second application examined the effect of intermittent hypoxia and a diet of advanced glycation end-products on element distribution in the brain. The most intriguing results were seen in the images for  $^{59}\text{Co}$ . A 100-fold elevation in the concentrations of  $^{59}\text{Co}$  was observed between mice exposed to intermittent hypoxia, those in a control environment and wild-type mice not exposed to the experiment's settings.

An examination into the use of  $\text{H}_2$  as a reaction gas was conducted. The improvement of the analytical performance of imaging experiments was considered for a range of masses with spectral interferences, including the  $^{40}\text{Ar}^{16}\text{O}^+$  spectral interference on  $^{56}\text{Fe}^+$ . At low ( $< 1.0 \text{ mL min}^{-1}$ )  $\text{H}_2$  flow rates, greater spectral interference due to  $\text{H}^+$  adducts were observed for  $^{57}\text{Fe}$  than with the reaction mode off. At higher flow rates, up to  $3.0 \text{ mL H}_2$  per minute, the spectral interferences were reduced leading to an improvement in the limits of analysis for masses with O- and N-based polyatomic interferences.

EBI is typically performed using spatial resolutions of  $30 \mu\text{m} \times 30 \mu\text{m}$  and above. Higher resolution imaging is desirable for many biological applications. As a culmination of the project, the combination of the use of improved matrix-matched tissue standards with the use of the reaction cell and increased image acquisition speeds was employed. The

combination of improved parameters resulted in a high quality image of the area of the brain including the substantia nigra being prepared at a resolution of  $6\ \mu\text{m} \times 6\ \mu\text{m}$  for  $^{56}\text{Fe}$ .